Cell Reports
Physical Science

CellPress
OPEN ACCESS

Article

Significant charge transport effects due to subtle molecular changes in nitroxide radical single crystals

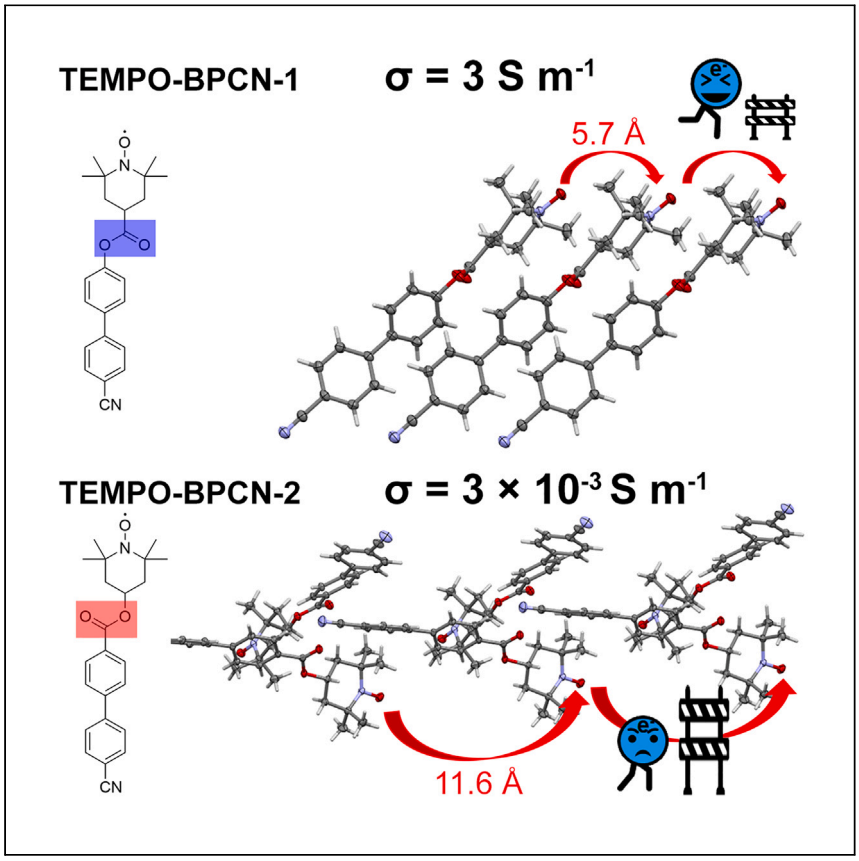

Liang and Hsu et al. report two nitroxide radical-based materials with similar molecular structures, but the subtle molecular difference between the two materials leads to a 1,000-fold difference in their electrical conductivities. Experimental structural analysis and simulations of charge transport reveal the underlying mechanism of this stark difference in performance.

Zihao Liang, Sheng-Ning Hsu, Ying Tan, ..., Letian Dou, Brett M. Savoie, Bryan W. Boudouris

boudouris@purdue.edu

Highlights

A nonconjugated radical small molecule with high electrical conductivity is synthesized

Huge charge transport difference between two structurally similar molecules is observed

Different charge transport rates for the two radical single crystals are interrogated

Liang et al., Cell Reports Physical Science 4, 101409
May 17, 2023
https://doi.org/10.1016/j.xcrp.2023.101409

Cell Reports
Physical Science

CellPress
OPEN ACCESS

Article

Significant charge transport effects due to subtle molecular changes in nitroxide radical single crystals

Zihao Liang,[1,4] Sheng-Ning Hsu,[1,4] Ying Tan,[1] Hamas Tahir,[1] Ho Joong Kim,[1] Kangying Liu,[2] Jacob F. Stoehr,[1] Matthias Zeller,[2] Letian Dou,[1,3] Brett M. Savoie,[1] and Bryan W. Boudouris[1,2,5,*]

SUMMARY

Radical-containing materials have received renewed interest due to their charge-conducting properties. However, most work focuses on macromolecules, while less attention has been paid to radical-containing small molecules. Here, we quantify the electrical conductivity in two organic radical single crystals and demonstrate that a subtle change in atomic connectivity drastically alters the macroscopic electronic properties of the materials. One radical crystal has an electrical conductivity of ~3 S m^{-1}, which is the among the highest values for nonconjugated radical conductors over a 1 μm scale. However, the other radical crystal has a 1,000-fold lower conductivity, despite their extremely similar molecular structures. The temperature-dependent conductivity follows the variable range hopping mechanism for both radical crystals, and the difference in effective charge mobility is the reason for the conductivity difference. These results present a clear picture of the design rules and charge transport mechanism for radical-based small-molecule materials.

INTRODUCTION

Nonconjugated radical polymers and small molecules are employed as conducting materials in many organic electronic devices, including electrolyte-supported devices[1–10] and solid-state electronic devices,[11–20] because of their charge transport and redox-active open-shell properties.[21–25] In radical polymer-based conductors, charge is transported through a series of oxidation-reduction reactions between the electronically active open-shell sites.[26–30] In fact, macromolecules with nonconjugated backbones and stable radical pendant groups can have impressive charge transport capabilities.[31,32] For instance, poly(4-glycidyloxy-2,2,6,6-tetramethylpiperidine-1-oxyl) (PTEO) has achieved a thin film electronic conductivity of ~20 S m^{-1}.[33] Despite this success of nonconjugated radical polymers as solid-state charge conductors and the excellent synthetic and magnetic work associated with small-molecule radical species,[34–47] the charge transport properties of nonconjugated open-shell small molecules have received less attention. With well-defined structures and the absence of grain boundaries, macroscopic charge transport phenomena are more easily described for single crystals relative to amorphous radical polymer thin films. Among various open-shell species, the 2,2,6,6-tetramethylpiperidin-1-oxyl (TEMPO) radical has received the most interest as an open-shell conductor because of its stability, relatively straightforward synthetic chemistry, and commercial availability. However, reports on the electrical conductivity values in radical small-molecule single crystals are not frequent.[48,49] Furthermore, the impact of molecular packing and arrangement of molecules within the crystals are

[1]Charles D. Davidson School of Chemical Engineering, Purdue University, 480 W Stadium Avenue, West Lafayette, IN 47907, USA

[2]Department of Chemistry, Purdue University, 560 Oval Drive, West Lafayette, IN 47907, USA

[3]Birck Nanotechnology Center, Purdue University, West Lafayette, IN 47907, USA

[4]These authors contributed equally

[5]Lead contact

*Correspondence: boudouris@purdue.edu

https://doi.org/10.1016/j.xcrp.2023.101409

often ignored. Therefore, it is important to quantify the charge transport properties of radical molecules with different crystal structures across a broader range of systems to elucidate the fundamental physical chemistry associated with solid-state charge transfer in nonconjugated open-shell small molecules.

Moreover, stable organic radicals that respond to magnetic fields are promising building blocks of magnetically active materials.[50–53] These open-shell materials are usually paramagnetic under ambient temperatures because of their unpaired electrons that respond to the external magnetic field and align their net moment in the same direction.[54,55] This magnetic ordering may affect the radical-based materials to change electrical resistance when a magnetic field is applied.[56–60] Previously, huge positive magnetoresistances were observed in a TEMPO-based single molecular junction setup, which shows the potential of the ability to tune the charge transport of radical conductors by external magnetic fields.[60] However, a more complete picture of how the charge transport is impacted by magnetic fields in organic radical-based materials is needed.

Motivated by these two guiding questions, we designed and synthesized two targeted radical-containing small molecules to establish the physical phenomena associated with their electrical conductivity and the magnetic properties in the single crystals grown from solution. In particular, 4′-cyano-[1,1′-biphenyl]-4-yl 1-hydroxyl-2,2,6,6-tetramethylpiperidine-4-carboxylate (TEMPO-BPCN-1) and 1-hydroxyl-2,2,6,6-tetramethylpiperidin-4-yl 4′-cyano-[1,1′-biphenyl]-4-carboxylate (TEMPO-BPCN-2), two rod-shaped molecules that are composed of a TEMPO moiety and a rigid cyano-biphenyl moiety, were synthesized. The two molecules are structurally similar, with the single differentiation being the direction of the ester bond that connects the TEMPO and cyano-biphenyl moieties. The rigid, rod-like biphenyl group endows both molecules with a strong tendency to grow into needle-like single crystals through an anti-solvent vapor diffusion method. The TEMPO-BPCN-1 single crystal has an electrical conductivity of $\sim$3 S m^{-1} at room temperature. However, the TEMPO-BPCN-2 single crystal has a 1,000-fold lower electrical conductivity. This huge difference is a result of the difference in the spatial arrangement of the radical moieties in their crystal lattices. That is, the nearest radical-radical distance along the conductivity measurement direction in a TEMPO-BPCN-1 crystal is almost half of that in TEMPO-BPCN-2. In addition, kinetic Monte Carlo simulations reveal that electron hopping is more efficient in TEMPO-BPCN-1 crystals, and this leads to higher effective charge mobility. The correlation of the conductivity with temperature across a large window (i.e., from 10 K < T < 340 K) fits well to the variable range hopping (VRH) model. Moreover, the electrical resistance in both single crystals changes with external magnetic fields, and the correlation of resistivity change with magnetic field strength fits well to the magnetoresistance model in the region of VRH conduction. Therefore, this work utilizes two TEMPO radical-based single crystals as a platform to elucidate the charge transport mechanism in nonconjugated radical-based conductors and highlights the potential of organic radical-based materials in electronic applications.

RESULTS AND DISCUSSION

Synthesis of well-defined small-molecule radicals

The radical molecules (i.e., TEMPO-BPCN-1 and TEMPO-BPCN-2) were synthesized through a Steglich esterification reaction at room temperature (Figure 1A). The successful synthesis of the product was confirmed by ^{1}H nuclear magnetic resonance (NMR) spectroscopy and high-resolution mass spectrometry (Figures S1–S4). A

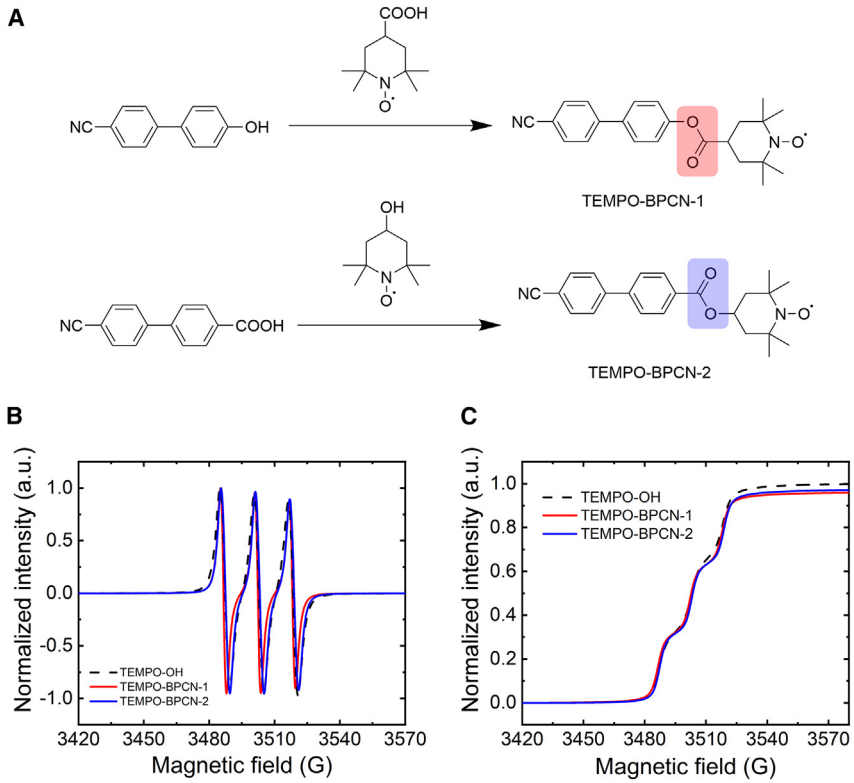

Figure 1. Synthesis of TEMPO-BPCN radical molecules

(A) Synthesis of TEMPO-BPCN molecules through a Steglich esterification reaction. The molecular difference between the two molecules is highlighted in red and blue.

(B) The first derivative EPR spectra of TEMPO-BPCN-1 (red line), TEMPO-BPCN-2 (blue line), and the TEMPO-OH standard (black dashed line), which confirm the existence of the TEMPO radical on the TEMPO-BPCN molecules.

(C) The doubly integrated EPR spectra of TEMPO-BPCN-1 (red line), TEMPO-BPCN-2 (blue line), and the TEMPO-OH standard (black dashed line).

triplet hyperfine splitting pattern was observed in the first derivative electron paramagnetic resonance (EPR) spectra, which confirms the presence of the nitroxide radical moiety on both molecules (Figure 1B). Furthermore, the radical loadings of all potential open-shell sites of TEMPO-BPCN-1 and TEMPO-BPCN-2 were calculated to be ~96% and ~97%, respectively, when 4-hydroxy-TEMPO (TEMPO-OH) was used as the standard (Figure 1C). The radical contents of the TEMPO-BPCN molecules were calculated by comparing the intensity of the doubly integrated spectra of the TEMPO-BPCN solution and the TEMPO-OH standard solution, and the radical content of the TEMPO-OH standard is defined to be 100%. The high radical contents in both molecules are a prerequisite toward achieving high electrical conductivity in the macroscopic materials.

Structures and physical properties of the radical crystals

Although the two molecules have similar chemical structures and are only differentiated by the direction of the ester bond that connects the cyno-biphenyl group and the TEMPO moiety, the structural difference in the single crystals is striking. The crystal structure of the solution-grown TEMPO-BPCN-1 (α-polymorph) is monoclinic ($P2_1/c$) with lattice parameters of a = 5.71 Å, b = 14.63 Å, and c = 24.22 Å and $\alpha = 90°$, $\beta = 92°$, and $\gamma = 90°$ (Figure 2A). The crystal structure of TEMPO-BPCN-2 is tetragonal ($P4_1$) with lattice parameters of a = 11.60 Å, b = 11.60 Å, and c = 14.82 Å

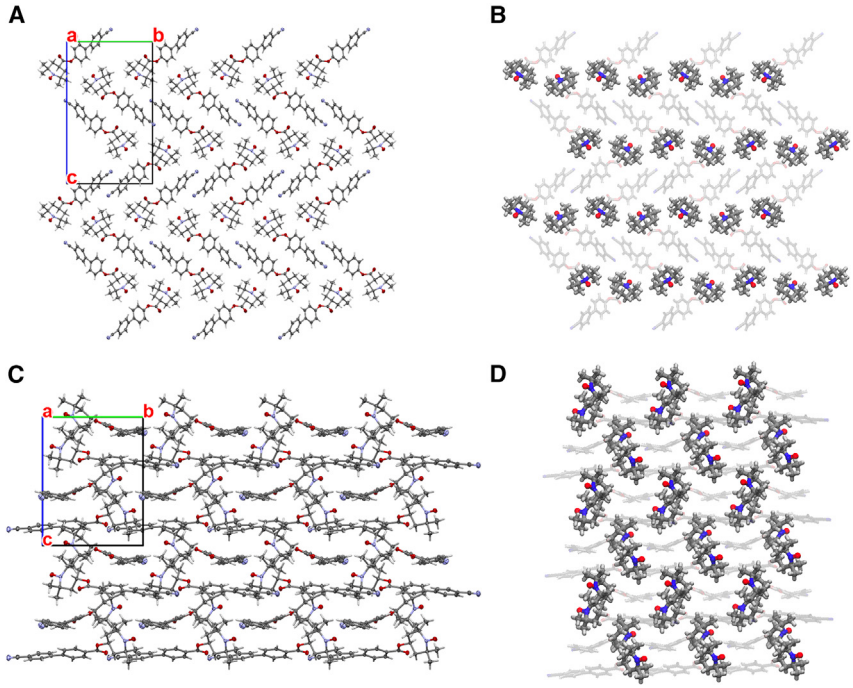

Figure 2. Molecular packing and spatial arrangements of radical moieties of TEMPO-BPCN radical molecules in their crystal structures

(A and C) Single-crystal structures of (A) TEMPO-BPCN-1 (α-polymorph) and (C) TEMPO-BPCN-2. The crystal cell b and c axes are shown in green and blue, respectively, and the a axis is perpendicular to the plane.

(B and D) The spatial arrangement of the TEMPO radical moieties in the crystal structure of (B) TEMPO-BPCN-1 (α-polymorph) and (D) TEMPO-BPCN-2. The TEMPO radical groups align into zigzag layers in the TEMPO-BPCN-1 single crystals and pack in dense cubes in the TEMPO-BPCN-2 single crystals.

and $\alpha = 90°$, $\beta = 90°$, and $\gamma = 90°$ (Figure 2C). Because the TEMPO radical moieties are key to charge transport, the spatial arrangement of the radical groups inside the crystal structures of the TEMPO-BPCN-1 and TEMPO-BPCN-2 are visualized in Figures 2B and 2D, respectively. The TEMPO radical groups align into zigzag layers in the TEMPO-BPCN-1 crystals, while the TEMPO radical groups pack in dense cubes in the TEMPO-BPCN-2 crystals. The radical site densities are 1.98×10^{21} and 2.01×10^{21} cm^{-3} for TEMPO-BPCN-1 and TEMPO-BPCN-2, respectively, indicating only the slightest difference between the radical content of the material is present. Density functional theory (DFT) calculations show that a swap of the two molecules in the crystal lattices results in a significant increase of the energy of the system (i.e., it requires 2.7 eV to force TEMPO-BPCN-2 into the lattice of TEMPO-BPCN-1 and 3.4 eV to force TEMPO-BPCN-1 into the lattice of TEMPO-BPCN-2), which suggests that a slight change in the molecular structure could lead to a complete rearrangement of the crystal structures (Figure S5; Table S1). In both crystal structures, the radical moieties are arranged periodically, which is promising in terms of charge transport. Hirshfeld surface analysis also indicates that relatively strong and localized intermolecular interactions exist on the nitroxide moieties of both TEMPO-BPCN-1 and TEMPO-BPCN-2 molecules (Figure S6).

The melting and crystallization behavior of TEMPO-BPCN-1 highlights a unique aspect of the structure of this material. The solution-grown TEMPO-BPCN-1 single crystals (α-polymorph) melt at 140°C during a first heating cycle, as determined

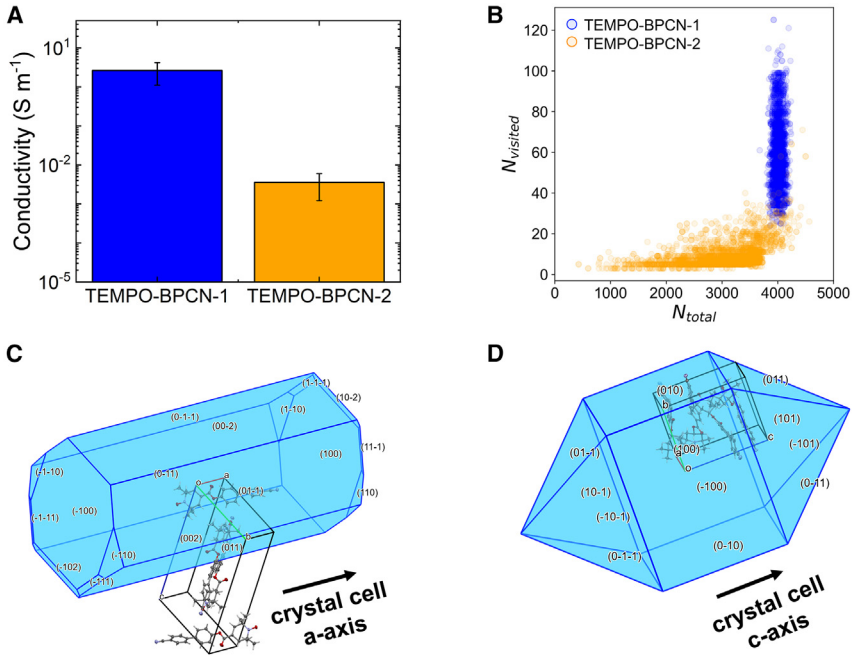

Figure 3. Difference in charge transport capabilities between TEMPO-BPCN radical molecules

(A) Room temperature electrical conductivity values of TEMPO-BPCN-1 (α-polymorph) and TEMPO-BPCN-2 single crystals. The average electrical conductivity and standard deviation values were calculated across three testing samples for both TEMPO-BPCN-1 and TEMPO-BPCN-2.

(B) The count of distinctly visited hopping sites and the total hopping sites in α-polymorph TEMPO-BPCN-1 (blue) and TEMPO-BPCN-2 (orange) single crystals. The computation includes 200 kinetic Monte Carlo (kMC) runs.

(C and D) The calculated Bravais, Friedel, Donnay, and Harker (BFDH) theoretical crystal morphology and a unit cell of (C) TEMPO-BPCN-1 (α-polymorph) and (D) TEMPO-BPCN-2. The long axis of the single crystal corresponds to direction of the a axis of the unit cell in TEMPO-BPCN-1 and the c axis of the unit cell in TEMPO-BPCN-2. In both crystal structures, red, blue, gray, and white were used to represent the oxygen, nitrogen, carbon, and hydrogen atoms, respectively.

using differential scanning calorimetry (DSC) and as shown in Figure S7. However, recrystallization during the first cooling occurs at 90°C, which is a different polymorph (β-polymorph). In the following heating and cooling DSC cycles, only the β-polymorph was observed. The crystal structure of the thermally grown β-polymorph is again monoclinic ($P2_1/c$), but the lattice parameters differ with a = 8.66 Å, b = 22.87 Å, and c = 20.76 Å and α = 90°, β = 95°, and γ = 90° forming those of α-polymorph. The densities of the unit cells for the two polymorphs are similar, 1.239 g cm^{-3} for the α-polymorph at 150 K and 1.251 g cm^{-3} for the β-polymorph at 150 K, indicating no difference in packing efficiency between the two polymorphs. The biphenyl rings of the TEMPO-BPCN molecules in the α-polymorph are twisted, while they are coplanar in the β-polymorph. The TEMPO-BPCN-2 crystals melt at 208°C, and the molecules underwent chemical decomposition while they were in the melting process.

Subtle molecular discrepancy and big difference in electrical conductivity

The two radical single crystals showed an orders-of-magnitude difference in charge transport capabilities. The TEMPO-BPCN-1 single crystal (α-polymorph) showed a high electrical conductivity of ~3 S m^{-1} at 300 K, which is the highest macroscopic conductivity value in nonconjugated radical conductors reported to date (Figure 3A). However, the single-crystal conductivity of TEMPO-BPCN-2 was about 1,000-fold

lower at 3×10^{-3} S m^{-1} at the same temperature. The average conductivity values and standard deviation at room temperature were calculated from three replica of samples. Kinetic Monte Carlo (kMC) simulations support these experimental observations. Figure 3B depicts the statistical distribution of the number of distinctly visited hopping sites and the total number of electron hops from 200 runs of kMC simulations. In TEMPO-BPCN-2, only 10 distinct sites were visited during the entire process because the bundled sites resulted in local charge traps that strongly limited charge transport. In comparison, the charge mobility of TEMPO-BPCN-1 is 4.35 times higher than TEMPO-BPCN-2, which is obtained from the mean-squared displacement (MSD) as shown in Figure S8 and Table S2. Across longer length scales, the charge transport of TEMPO-BPCN-1 will be even more effective than that of TEMPO-BPCN-2 due to the advantage in its charge transport mobility. This again demonstrates that a small change in the molecular structure results in very different radical site arrangements, which in turn significantly affects charge transport.

Moreover, the orders-of-magnitude difference in charge transport capability is backed by the difference in the nearest radical-radical distance along the long axis of single crystal. As the spin density visualization suggests, the spins are localized on the N–O bond from the TEMPO moiety for both the TEMPO-BPCN-1 (α-polymorph) and TEMPO-BPCN-2 crystals (Figure S9). Due to the hopping nature of charge transport in nonconjugated radicals, the spatial arrangements between the radical sites strongly affect the charge transport capabilities of the single crystals. The Bravais, Friedel, Donnay, and Harker (BFDH) theoretical crystal morphology was calculated from the unit cell for both TEMPO-BPCN molecules (Figures 3C and 3D).[61] The long axis of the TEMPO-BPCN-1 single crystal (α-polymorph) corresponds to the a axis of the unit cell, and the nearest TEMPO-TEMPO distance along the a axis was around 5.7 Å, which is predicted to be an acceptably close distance for efficient charge transport to occur in nonconjugated radical-based materials.[62,63] In comparison, the long axis of the TEMPO-BPCN-2 single crystal corresponds to the c axis of the unit cell, and the nearest TEMPO-TEMPO distance along the c axis was around 11.6 Å, which is almost twice the hopping distance of that in the TEMPO-BPCN-1 crystal lattice. This atomic-scale investigation reveals the possible reason behind the 1,000-fold difference in electrical conductivity between the two radical crystals.

Charge transport mechanism of radical single crystals

The single-crystal conductivities of both molecules increased with increasing temperatures, which is consistent with a thermally activated transport mechanism. Importantly, the activation energy provides further insights into the materials and their solid-state transport mechanism. If charge transport is dominated by a single pathway (i.e., nearest-neighbor transport), then the activation energy would be independent of temperature, and the conductivity is Arrhenian. However, in the single crystals, the activation energy was higher at elevated temperatures (Figure S10). Therefore, their electrical conductivity can be described by a VRH mechanism,[64–66] which is expressed as Equation 1:

$$\sigma = \sigma_0 \, e^{-(T_0/T)^{1/P}} \qquad \text{(Equation 1)}$$

Here, T, σ_0, and T_0 are the absolute temperature, a constant, and the characteristic temperature, respectively, and p is a fitting parameter. In the 3D Mott-VRH model, p = 4, and in the Efros-Shklovskii VRH (ES-VRH) model, p = 2. In the TEMPO-BPCN-1 single crystals, both VRH models fit well (Figure 4A). However, the 3D Mott-VRH

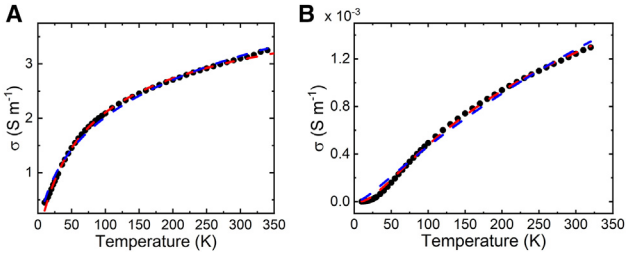

Figure 4. Charge transport mechanism of TEMPO-BPCN radical molecules

The electrical conductivity (black dots) of (A) TEMPO-BPCN-1 (α-polymorph) and (B) TEMPO-BPCN-2 single crystals across a temperature range of 10 K ≤ T ≤ 340 K as measured. The data were fit to the Efros-Shklovskii (dashed red line) and 3D Mott (dashed blue line) variable range hopping models.

model showed slight deviation from the experimental data in TEMPO-BPCN-2 single crystals (Figure 4B). The T_0 value obtained from the 3D Mott-VRH model is 1,146 K for TEMPO-BPCN-1 and 3.1×10^4 K for TEMPO-BPCN-2, while the T_0 values obtained from the ES-VRH model are 80 K for TEMPO-BPCN-1 and 523 K for TEMPO-BPCN-2. Because the T_0 values do not carry specific physical meanings by themselves, we converted these values into activation energies (E_a). The calculated E_a values based on T_0 values from the 3D Mott-VRH model are 9.04 and 20.6 meV at 300 K for TEMPO-BPCN-1 and TEMPO-BPCN-2, respectively, while the E_a values at 300 K calculated from the ES-VRH model are 122.3 and 312.6 meV for TEMPO-BPCN-1 and TEMPO-BPCN-2, respectively (Figure S11). All E_a values are at the same order of magnitude with 3 kT (~77.6 meV at 300 K), which implies that the thermal energy is sufficient to trigger the hopping transport.[67] For both 3D Mott- and ES-VRH models, the derived E_a values of TEMPO-BPCN-1 are substantially lower than those of TEMPO-BPCN-2, which correlates well with the 1,000-fold differences in electrical conductivities between the two radical crystals. The VRH behavior of these materials indicate that the macroscopic electrical conductivity of crystalline TEMPO species is attributed to multiple charge transport pathways. The variable hopping ranges and E_a values imply that multiple pathways dominate charge transport at different temperatures. The p value in Equation 1 is determined by the behavior of the density of states (DOS) near the Fermi level (μ) (Figure S12; Note S1). Furthermore, the single-crystal conductivities of two other TEMPO-based radical conductors in a recent report also follow VRH model, which indicates that the VRH model is a general charge transport mechanism in nonconjugated radical systems.[68] Therefore, we propose that the VRH model could describe most of the macroscopic solid-state charge transport of the nonconjugated radical species.

Charge transport in the presence of magnetic fields

The electrical conductivity in these radical single crystals varied when magnetic fields were applied onto the device, and the magnetic field-dependent charge transport behavior also follows the VRH mechanism. Here, magnetic fields with strengths of B were applied perpendicularly to the transport direction, and the electrical resistances under magnetic fields were measured (Figure S13). The calculation of magnetoresistance (MR) is described in Equation 2.

$$MR = \frac{\Delta R}{R} = \frac{R(B) - R(0)}{R(0)} \qquad \text{(Equation 2)}$$

Here, $R(B)$ and $R(0)$ are the electrical resistance in the presence and absence of a magnetic field with the strength of B, respectively. For both molecules, positive MR values were observed under all the testing temperatures, and the MR curves

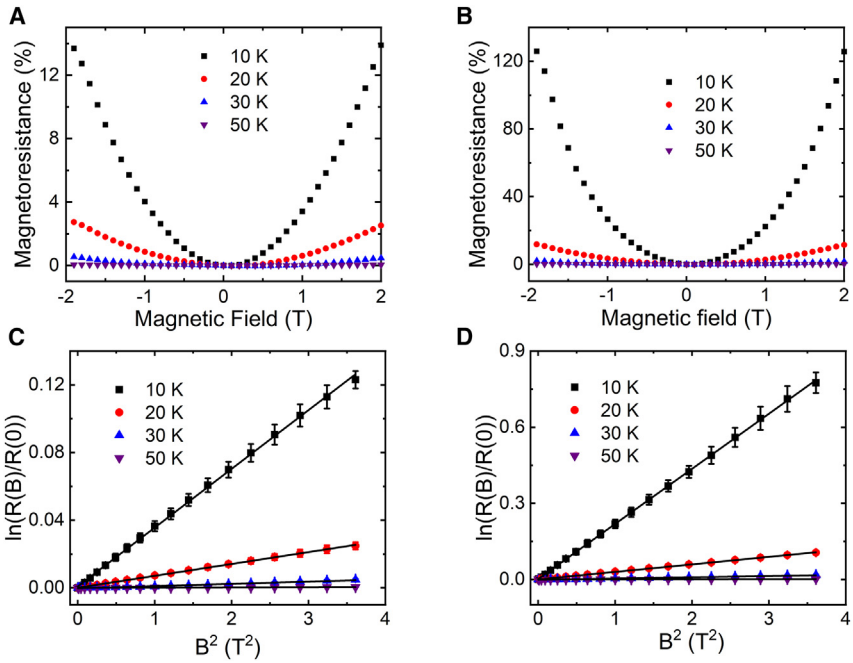

Figure 5. Charge transport behaviors of TEMPO-BPCN radical molecules under magnetic fields

(A and B) The electrical resistance in the crystals of (A) TEMPO-BPCN-1 and (B) TEMPO-BPCN-2 changes with an applied magnetic field of $-2\ T \leq B \leq 2\ T$. For all temperatures, the measurement started at −2 T, and for each data point, the magnetic field was equilibrated for 60 s.

(C and D) The natural log of $R(B)/R(0)$ under the square of magnetic field strength of (C) TEMPO-BPCN-1 and (D) TEMPO-BPCN-2 under temperatures of 10–50 K. The black curve shows the liner fit of this correlation. The error bars represent standard deviation around the mean of three repeated measurements.

were symmetric when the magnetic field was applied in both directions. For TEMPO-BPCN-1, the MR was ∼13% at 2 T and 10 K, and this is comparable to standard conjugated polymers at the same temperature (Figure 5A).[56] However, the MR dropped significantly as the temperature was increased above 10 K, with only 2.5% at T = 20 K and <1% for T >30 K. As for the TEMPO-BPCN-2 crystal, the MR was ∼120% at 10 K, which is 10 times higher than TEMPO-BPCN-1, and it dropped to 12% at 20 K, 2% at 30 K, and less than 1% above 30 K. This decrease is consistent with the fact that both TEMPO-BPCN-1 and TEMPO-BPCN-2 crystals exhibit paramagnetic behavior in the temperature range of 2–300 K (Figure S14), as their molar magnetic susceptibility (χ_m) vs. T dependence follows the Curie-Weiss law (Table S3).

In the VRH theory at low magnetic strength, the MR can be described as Equation 3:

$$\frac{R(B)}{R(0)} = e^{AB^2}, \text{where } A \propto \frac{a}{N} \qquad \text{(Equation 3)}$$

and a and N are the localization radius and carrier concentration, respectively. Because the localization radius is determined by the TEMPO radical, we assume the two TEMPO-BPCN molecules have the same localization radius. Thus, the calculated carrier concentration of TEMPO-BPCN-2 was approximately 16% of that of TEMPO-BPCN-1, a difference that can barely contribute to the three orders magnitude of difference in conductivities. Therefore, the charge carrier mobility, which is determined by how the radical sites are spatially arranged in the crystal lattice, is still the main reason for the huge difference in electrical conductivity. The plot of $\ln(R(B)/R(0))$ against B^2 for TEMPO-BPCN-1 and TEMPO-BPCN-2 are

shown in Figures 5C and 5D, respectively. All curves showed an excellent linear fit, which implies that both materials follow Equation 3 closely, which is consistent with the idea that VRH is the governing charge transport mechanism of nonconjugated radical species.

Two radical-based molecules with similar molecular structures were designed, synthesized, and crystallized. TEMPO-BPCN-1 single crystals showed the highest macroscopic electrical conductivities (i.e., ~3 S m^{-1}) in nonconjugated radical conductors reported to date. This is because the spatial arrangement of the radical groups in their crystal structures facilitates charge transport, as TEMPO-BPCN-2 single crystals only showed 1,000-fold lower electrical conductivities. This charge transport difference is also supported by kMC simulations, which reveals that electron hopping is more efficient in TEMPO-BPCN-1 crystals. The temperature-dependent conductivity follows the VRH mechanism, where the charge carriers are localized in the nonconjugated radical moieties on the molecules. This mechanism is also backed by the fact that the magnetic field-dependent electrical resistance in the radical crystals follows the MR model under the VRH mechanism. This work elucidates the charge transport mechanism in the nitroxide radical single crystals for the first time and points out the potential of the nonconjugated radical-based materials in electronic applications.

EXPERIMENTAL PROCEDURES

Resource availability

Lead contact

Further information and requests for resources should be directed to and will be fulfilled by the lead contact, Bryan W. Boudouris (boudouris@purdue.edu).

Materials availability

The experimental dataset and materials generated and/or analyzed during the current study are available from the lead contact upon reasonable request.

Data and code availability

All data supporting this study are available in the supplemental information. All single crystal X-ray structure files reported in this article have been deposited in the Cambridge Structure Database under deposition numbers CCDC: 2189453 (TEMPO-BPCN-1 α-polymorph), 2189454 (TEMPO-BPCN-1 β-polymorph), and 2216666 (TEMPO-BPCN-2). The crystallographic information files are also available as Data S1, S2, and S3. All computational data have been deposited at figshare under TEMPO BPCN Simulation Scripts Data. figshare. Dataset. https://doi.org/10.6084/m9.figshare.22577275.v1 and are publicly available as of the date of publication. This article does not report original code. Any additional information required to reanalyze the computational data reported in this article is available from the lead contact upon request.

Materials and general methods

All reagents were purchased from Sigma-Aldrich. Also, 4-carboxy-2,2,6,6-tetramethylpiperidin1-oxyl was purchased from TCI America. All chemicals were used as they were received. The melting and crystallization temperatures were evaluated using a TA Instruments Q20 Series DSC. In these experiments, all heating and cooling ramps occurred at a rate of 2°C min^{-1}. EPR spectroscopy data were obtained using a Bruker EPR-EMX spectrometer at room temperature. TEMPO-BPCN molecules were dissolved in chloroform at a concentration of 1 mg mL^{-1}, and the TEMPO-OH standards were prepared in the same way. The mass spectra

were obtained using a Thermo Finnigan LTQ orbitrap mass spectrometer with an electrospray ionization (ESI) probe, and positively charged ions were detected in the ESI mode. The ^{1}H NMR spectra were collected using a Bruker AV-III-400-HD NMR spectrometer using solutions of ~1% (by weight) materials in $CDCl_3$. The radical sites on the TEMPO-BPCN molecules were quenched using L-ascorbic acid prior to collecting the NMR spectra.[69] The scanning electron microscope (SEM) images were collected with FEI Teneo SEM (Everhart–Thornley detector, voltage = 5 kV, and working distance = 10 mm).

Synthesis of TEMPO-BPCN-1

The synthesis of TEMPO-BPCN-1 was modified from a previous report.[70] Briefly, in a 100 mL round-bottom flask, 4-carboxy-2,2,6,6-tetramethylpiperidin1-oxyl (220 mg, 1 mmol) and *N*,*N*′-dicyclohexylcarbodiimide (DCC) (247 mg, 1.2 mmol) were dissolved in 10 mL anhydrous dichloromethane (DCM). The mixture was stirred for 30 min, and a white precipitate was generated. Then, 4′-hydroxy-[1,1′-biphenyl]-4-carbonitrile (195 mg, 1 mmol) and 4-dimethylaminopyridine (DMAP) (12 mg, 0.1 mmol) were added, and the reaction mixture was stirred for 24 h at room temperature. Upon the completion of the reaction, the precipitate was removed by filtration, and the clear solution was collected and concentrated using a rotary evaporator. The mixture was purified by column chromatography on silica gel with hexane:ethyl acetate = 8:1 v/v serving as the eluent to recover 311 mg of the product as orange solid (yield = 82%). The ^{1}H NMR chemical shifts are (400 MHz, $CDCl_3$): δ 7.72 (d, 2H), 7.68 (d, 2H), 7.60 (d, J = 8.9 Hz, 2H), 7.20 (d, J = 8.5 Hz, 2H), 4.47 (s, 1H), 2.95 (tt, J = 12.6, 3.4 Hz, 1H), 2.06–1.94 (m, 2H), 1.79 (t, J = 13.2 Hz, 2H), 1.24 (d, J = 17.4 Hz, 12H).

Synthesis of TEMPO-BPCN-2

In this synthesis, 4′-cyano-[1,1′-biphenyl]-4-carboxylic acid (223 mg, 1 mmol) and DCC were added to a 100 mL round-bottom flask with 10 mL DCM. The mixture was stirred for 30 min, and precipitates were generated. Then, 4-hydroxy-2,2,6,6-tetramethylpiperidin1-oxyl (172 mg, 1 mmol) and DMAP (12 mg, 0.1 mmol) were added, and the reaction mixture was stirred for 24 h at room temperature. Upon the completion of the reaction, the precipitate was removed by filtration, and the clear solution was collected and concentrated using a rotary evaporator. The mixture was purified by column chromatography on silica gel with hexane:DCM = 8:1 v/v serving as the eluent to recover 260 mg of the product as orange solid (yield = 69%). The ^{1}H NMR chemical shifts are (400 MHz, $CDCl_3$): δ 8.14 (d, J = 8.2 Hz, 2H), 7.76 (d, J = 10.3 Hz, 4H), 7.67 (d, J = 8.3 Hz, 2H), 5.40–5.31 (m, 1H), 2.09 (dd, J = 12.7, 4.4 Hz, 2H), 1.78 (t, J = 11.8 Hz, 2H), 1.28 (d, J = 9.0 Hz, 12H).

Single-crystal growth

Single crystals of TEMPO-BPCN-1 in the α-polymorph and TEMPO-BPCN-2 were prepared using the anti-solvent vapor diffusion method (Figure S15). In a 7 mL glass vial, a saturated solution (i.e., TEMPO-BPCN-1 in ethyl acetate or TEMPO-BPCN-2 in chloroform) was loaded after passing it through a PTFE syringe filter with 0.45 μm pore size. Then, the inner vial was placed in a 20 mL scintillation vial, and a mixture of hexanes and ethyl ether (1:1, v/v) was loaded outside the inner vial. The setup was then capped tightly and placed in a cabinet with no disturbance for 5 days. Needle-like TEMPO-BPCN-1 and TEMPO-BPCN-2 single crystals with an orange color were obtained. Single crystals of TEMPO-BPCN-1 in the β-polymorph were prepared by cooling isotropic liquids of TEMPO-BPCN-1 on a MiTeGen micromesh sample holder in real time on the goniometer head of a Bruker Quest diffractometer (Tables S4–S6; Note S2).

Device fabrication and electrical conductivity measurements

The single crystals, along with some of the mother solution, were removed from the vial using a micropipette with a trimmed tip and dropped on a silicon substrate with a thermally grown silicon dioxide layer. Then, the surface of the dropped crystals was cleaned by spin coating an additional ethyl acetate at 1,000 rpm for 30 s. Using a silver wire (radius ~140 μm) as a shadow mask, 100 nm gold and 400 nm silver were deposited as electrodes by thermal evaporation (Figure S16A).[71] The resistance (R) values were determined by sweeping voltage and measuring current (I-V curves) and then taking the slopes of voltage versus current plot as the corresponding resistance base on Ohm's law (Figure S16B). All I-V curves were linear. The electrical conductivity of the sample was determined using the device channel length (L) and crystal width (W), as characterized using optical microscopy with the following equation, assuming the sample width and sample height are approximately equal.

$$\sigma = \frac{L}{W^2 R} \quad \text{(Equation 4)}$$

The validity of this assumption was double checked with SEM. Example SEM images of the TEMPO-BPCN-1 and TEMPO-BPCN-2 devices with a 45° tilted angle are shown in Figure S17. The varying temperature conductivity measurements were performed by measuring the electrical resistances under different temperature setpoints. To ensure thermal equilibrium was reached, the samples were held for 10 min at the new temperature setpoint before I-V measurements were collected. The MR was obtained by measuring resistances under varying magnetic fields under constant voltage bias of 1 V. Each resistance value acquired using a different magnet field was determined by averaging 50 data points (number of power line cycles = 1).

Computational methods

Periodic DFT calculations were performed within plane-wave basis sets and projector augmented-wave (PAW) pseudopotentials as implemented in the Vienna ab initio simulation package (VASP).[72–76] VASP input files were generated by the VASPKIT program.[77] Revised Perdew-Burke-Ernzerhof (PBE) for solids (PBEsol) was used as the generalized gradient approximation (GGA) exchange-correlation functional. A tight K-point mesh with maximum K-point distance set to $2\pi \times 0.030$ Å^{-1} was generated using a Γ-centered Monkhorst-Pack scheme. The required SCF convergence criterion was a minimum of 10^{-8} eV. Hirshfeld surface analysis was performed using the build-in package in CrystalExplorer.[78]

kMC simulations were applied to analyze charge transport in the superlattice conformation of the two molecules.[79] The single-crystal structures given by X-ray diffraction were used as the starting point to create a superlattice of 10 × 10 × 10 crystal size for analysis. Independent charge transfer sites were defined as all nitroxide heads in the TEMPO radical that potentially participated in charge transport. Within the KMC framework, given a 0.5 ns charge hopping time, sites are held fixed and charge transfer rates decay exponentially with radical distance. The self-diffusion coefficient (D) was obtained by the MSD slope of the charges. The mobility (μ) was obtained from the diffusivity using the Einstein relation, where e is the unit electron charge (Equation 5).

$$\mu = \frac{eD}{k_B T} \quad \text{(Equation 5)}$$

Magnetic measurements

The χ_m measurements for TEMPO-BPCN-1 (both in α- and β-polymorphs) and TEMPO-BPCN-2 were carried out in a Quantum Design superconducting quantum

interference device (SQUID) magnetometer with a sensitivity of 5×10^{-8} emu. The samples were prepared by placing ~5 mg of the material of interest in a clean, dry polycarbonate capsule. The vibrating sample mode was utilized for all the measurements. Initially, a small magnetic field of 1,000 Oe was applied, and the temperature-dependent susceptibility was recorded while the sample was cooled from 300 to 2 K. The χ_m was corrected for the contribution of the sample holder, and the contribution from the diamagnetic closed-shell portions in the molecules was also corrected using Pascal's constants.

SUPPLEMENTAL INFORMATION

Supplemental information can be found online at https://doi.org/10.1016/j.xcrp.2023.101409.

ACKNOWLEDGMENTS

This work was supported by the US Department of Energy, Office of Science, Basic Energy Sciences, under award DE-SC0021967, and we thank the Department of Energy for this generous support. The work on the single-crystal X-ray diffractions was supported by the National Science Foundation through the Major Research Instrumentation Program under award CHE 1625543. The work on mass spectroscopy was supported in part by the Research Instrumentation Center in the Department of Chemistry at Purdue University.

AUTHOR CONTRIBUTIONS

Z.L. and S.-N.H. contributed equally to this work. Z.L. and S.-N.H. prepared the crystals and characterized the electrical properties. H.T. conducted the magnetic characterizations. Y.T. performed charge transport simulation. K.L. conducted EPR experiments. H.J.K. assisted with the electrical property testing. J.F.S. assisted with the synthesis of chemicals. M.Z. analyzed the single-crystal structures. B.W.B. conceived the idea and led the project with discussion from L.D. and B.M.S. Z.L., S.-N.H., and B.W.B. prepared the first version of the manuscript, and all authors contributed to the discussion on the results and the final version.

DECLARATION OF INTERESTS

The authors declare no competing interests.

Received: February 6, 2023
Revised: March 27, 2023
Accepted: April 13, 2023
Published: May 5, 2023

REFERENCES

1. Kim, H.J., Perera, K., Liang, Z., Bowen, B., Mei, J., and Boudouris, B.W. (2022). Radical polymer-based organic electrochemical transistors. ACS Macro Lett. *11*, 243–250. https://doi.org/10.1021/acsmacrolett.1c00695.

2. Xie, Y., Zhang, K., Yamauchi, Y., Oyaizu, K., and Jia, Z. (2021). Nitroxide radical polymers for emerging plastic energy storage and organic electronics: fundamentals, materials, and applications. Mater. Horiz. *8*, 803–829. https://doi.org/10.1039/d0mh01391a.

3. He, J., Mukherjee, S., Zhu, X., You, L., Boudouris, B.W., and Mei, J. (2018). Highly transparent crosslinkable radical copolymer thin film as the ion storage layer in organic electrochromic devices. ACS Appl. Mater. Interfaces *10*, 18956–18963. https://doi.org/10.1021/acsami.8b03235.

4. Yonekuta, Y., Susuki, K., Oyaizu, K., Honda, K., and Nishide, H. (2007). Battery-inspired, nonvolatile, and rewritable memory architecture: a radical polymer-based organic device. J. Am. Chem. Soc. *129*, 14128–14129. https://doi.org/10.1021/ja075553p.

5. Suga, T., Pu, Y.J., Kasatori, S., and Nishide, H. (2007). Cathode- and anode-active poly(nitroxylstyrene)s for rechargeable batteries: P- and n-type redox switching via substituent effects. Macromolecules *40*, 3167–3173. https://doi.org/10.1021/ma0628578.

6. Oyaizu, K., Kawamoto, T., Suga, T., and Nishide, H. (2010). Synthesis and charge transport properties of redox-active nitroxide polyethers with large site density. Macromolecules *43*, 10382–10389. https://doi.org/10.1021/ma1020159.

7. Nishide, H., Iwasa, S., Pu, Y.J., Suga, T., Nakahara, K., and Satoh, M. (2004). Organic radical battery: nitroxide polymers as a cathode-active material. Electrochim. Acta *50*, 827–831. https://doi.org/10.1016/j.electacta.2004.02.052.

8. Suga, T., Ohshiro, H., Sugita, S., Oyaizu, K., and Nishide, H. (2009). Emerging n-type redox-active radical polymer for a totally organic polymer-based rechargeable battery. Adv. Mater. *21*, 1627–1630. https://doi.org/10.1002/adma.200803073.

9. Mukherjee, S., and Boudouris, B.W. (2017). Design of a three-state switchable chromogenic radical-based moiety and its translation to molecular logic systems. Mol. Syst. Des. Eng. *2*, 159–164. https://doi.org/10.1039/c7me00010c.

10. Chung, J., Khot, A., Savoie, B.M., and Boudouris, B.W. (2020). 100th anniversary of macromolecular science viewpoint: recent advances and opportunities for mixed ion and charge conducting polymers. ACS Macro Lett. *9*, 646–655. https://doi.org/10.1021/acsmacrolett.0c00037.

11. Zhang, Y., Basel, T.P., Gautam, B.R., Yang, X., Mascaro, D.J., Liu, F., and Vardeny, Z.V. (2012). Spin-enhanced organic bulk heterojunction photovoltaic solar cells. Nat. Commun. *3*, 1043. https://doi.org/10.1038/ncomms2057.

12. Wilcox, D.A., and Boudouris, B.W. (2020). Modifying field-effect transistor response in a conjugated polymer upon the addition of radical dopants. Thin Solid Films *714*, 138391. https://doi.org/10.1016/j.tsf.2020.138391.

13. Rostro, L., Baradwaj, A.G., and Boudouris, B.W. (2013). Controlled radical polymerization and quantification of solid state electrical conductivities of macromolecules bearing pendant stable radical groups. ACS Appl. Mater. Interfaces *5*, 9896–9901. https://doi.org/10.1021/am403223s.

14. Rostro, L., Galicia, L., and Boudouris, B.W. (2015). Suppressing the environmental dependence of the open-circuit voltage in inverted polymer solar cells through a radical polymer anodic modifier. J. Polym. Sci., Part B: Polym. Phys. *53*, 311–316. https://doi.org/10.1002/polb.23640.

15. Zheng, L., Mukherjee, S., Wang, K., Hay, M.E., Boudouris, B.W., and Gong, X. (2017). Radical polymers as interfacial layers in inverted hybrid perovskite solar cells. J. Mater. Chem. A *5*, 23831–23839. https://doi.org/10.1039/c7ta07732g.

16. Joo, Y., Huang, L., Eedugurala, N., London, A.E., Kumar, A., Wong, B.M., Boudouris, B.W., and Azoulay, J.D. (2018). Thermoelectric performance of an open-shell donor-acceptor conjugated polymer doped with a radical-containing small molecule. Macromolecules *51*, 3886–3894. https://doi.org/10.1021/acs.macromol.8b00582.

17. Tomlinson, E.P., Willmore, M.J., Zhu, X., Hilsmier, S.W.A., and Boudouris, B.W. (2015). Tuning the thermoelectric properties of a conducting polymer through blending with open-shell molecular dopants. ACS Appl. Mater. Interfaces *7*, 18195–18200. https://doi.org/10.1021/acsami.5b05860.

18. Sung, S.H., Bajaj, N., Rhoads, J.F., Chiu, G.T., and Boudouris, B.W. (2016). Radical polymers improve the metal-semiconductor interface in organic field-effect transistors. Org. Electron. *37*, 148–154. https://doi.org/10.1016/j.orgel.2016.06.020.

19. Oyaizu, K., and Nishide, H. (2009). Radical polymers for organic electronic devices: a radical departure from conjugated polymers? Adv. Mater. *21*, 2339–2344. https://doi.org/10.1002/adma.200803554.

20. Zhang, K., Monteiro, M.J., and Jia, Z. (2016). Stable organic radical polymers: synthesis and applications. Polym. Chem. *7*, 5589–5614. https://doi.org/10.1039/c6py00996d.

21. Akkiraju, S., Vergados, J., Hoagland, L., Lu, Z., Anandan, V., and Boudouris, B.W. (2021). Design of mixed electron- and ion-conducting radical polymer-based blends. Macromolecules *54*, 5178–5186. https://doi.org/10.1021/acs.macromol.1c00113.

22. Chen, Z.X., Li, Y., and Huang, F. (2021). Persistent and stable organic radicals: design, synthesis, and applications. Chem *7*, 288–332. https://doi.org/10.1016/j.chempr.2020.09.024.

23. Tan, Y., Casetti, N.C., Boudouris, B.W., and Savoie, B.M. (2021). Molecular design features for charge transport in nonconjugated radical polymers. J. Am. Chem. Soc. *143*, 11994–12002. https://doi.org/10.1021/jacs.1c02571.

24. Chi, T., Akkiraju, S., Liang, Z., Tan, Y., Kim, H.J., Zhao, X., Savoie, B.M., and Boudouris, B.W. (2021). Design of an n-type low glass transition temperature radical polymer. Polym. Chem. *12*, 1448–1457. https://doi.org/10.1039/d0py01645d.

25. Rostro, L., Wong, S.H., and Boudouris, B.W. (2014). Solid state electrical conductivity of radical polymers as a function of pendant group oxidation state. Macromolecules *47*, 3713–3719. https://doi.org/10.1021/ma500626t.

26. Wingate, A.J., and Boudouris, B.W. (2016). Recent advances in the syntheses of radical-containing macromolecules. J. Polym. Sci., Part A: Polym. Chem. *54*, 1875–1894. https://doi.org/10.1002/pola.28088.

27. Ji, L., Shi, J., Wei, J., Yu, T., and Huang, W. (2020). Air-stable organic radicals: new-generation materials for flexible electronics? Adv. Mater. *32*, e1908015. https://doi.org/10.1002/adma.201908015.

28. Wang, S., Easley, A.D., and Lutkenhaus, J.L. (2020). 100th anniversary of macromolecular science viewpoint: fundamentals for the future of macromolecular nitroxide radicals. ACS Macro Lett. *9*, 358–370. https://doi.org/10.1021/acsmacrolett.0c00063.

29. Hansen, K.A., and Blinco, J.P. (2018). Nitroxide radical polymers-A versatile material class for high-Tech applications. Polym. Chem. *9*, 1479–1516. https://doi.org/10.1039/c7py02001e.

30. Mukherjee, S., and Boudouris, B.W. (2017). Organic Radical Polymers: New Avenues in Organic Electronics (Springer).

31. Price, J.T., Paquette, J.A., Harrison, C.S., Bauld, R., Fanchini, G., and Gilroy, J.B. (2014). 6-Oxoverdazyl radical polymers with tunable electrochemical properties. Polym. Chem. *5*, 5223–5226. https://doi.org/10.1039/c4py00829d.

32. Jähnert, T., Häupler, B., Janoschka, T., Hager, M.D., and Schubert, U.S. (2014). Polymers based on stable phenoxyl radicals for the use in organic radical batteries. Macromol. Rapid Commun. *35*, 882–887. https://doi.org/10.1002/marc.201300791.

33. Joo, Y., Agarkar, V., Sung, S.H., Savoie, B.M., and Boudouris, B.W. (2018). A nonconjugated radical polymer glass with high electrical conductivity. Science *359*, 1391–1395. https://doi.org/10.1126/science.aao7287.

34. Gallagher, N., Zhang, H., Junghoefer, T., Giangrisostomi, E., Ovsyannikov, R., Pink, M., Rajca, S., Casu, M.B., and Rajca, A. (2019). Thermally and magnetically robust triplet ground state diradical. J. Am. Chem. Soc. *141*, 4764–4774. https://doi.org/10.1021/jacs.9b00558.

35. Wang, W., Chen, C., Shu, C., Rajca, S., Wang, X., and Rajca, A. (2018). S = 1 tetraazacyclophane diradical dication with robust stability: a case of low-temperature one-dimensional antiferromagnetic chain. J. Am. Chem. Soc. *140*, 7820–7826. https://doi.org/10.1021/jacs.8b02415.

36. Hicks, R.G. (2007). What's new in stable radical chemistry? Org. Biomol. Chem. *5*, 1321–1338. https://doi.org/10.1039/b617142g.

37. Koivisto, B.D., and Hicks, R.G. (2005). The magnetochemistry of verdazyl radical-based materials. Coord. Chem. Rev. *249*, 2612–2630. https://doi.org/10.1016/j.ccr.2005.03.012.

38. Hicks, R.G., Lemaire, M.T., Thompson, L.K., Barclay, T.M., Box, P.O., Vw, B.C., Johns, S., Ab, N., and May, R.V. (2000). Strong ferromagnetic and antiferromagnetic exchange coupling between transition metals and coordinated verdazyl radicals. J. Am. Chem. Soc. *122*, 8077–8078. https://doi.org/10.1021/ja001627k.

39. Hicks, R.G. (2011). Switchable materials: a new spin on bistability. Nat. Chem. *3*, 189–191. https://doi.org/10.1038/nchem.997.

40. Sanz, C.A., McKay, Z.R., Maclean, S.W.C., Patrick, B.O., and Hicks, R.G. (2017). Synthesis and redox reactions of bis(verdazyl)palladium complexes. Dalton Trans. *46*, 12636–12644. https://doi.org/10.1039/c7dt02646c.

41. Johnston, C.W., McKinnon, S.D.J., Patrick, B.O., and Hicks, R.G. (2013). The first "kuhn verdazyl" ligand and comparative studies of its PdCl2 complex with analogous 6-oxoverdazyl ligands. Dalton Trans. *42*, 16829–16836. https://doi.org/10.1039/c3dt52191e.

42. McKinnon, S.D.J., Patrick, B.O., Lever, A.B.P., and Hicks, R.G. (2011). Electronic structure investigations of neutral and charged ruthenium Bis(β-diketonate) complexes of redox-active verdazyl radicals. J. Am. Chem. Soc. *133*, 13587–13603. https://doi.org/10.1021/ja204575u.

43. Zhang, H., Pink, M., Wang, Y., Rajca, S., and Rajca, A. (2022). High-spin S = 3/2 ground-state aminyl triradicals: toward high-spin oligo-aza nanographenes. J. Am. Chem. Soc. *144*, 19576–19591. https://doi.org/10.1021/jacs.2c09241.

44. Zhang, S., Pink, M., Junghoefer, T., Zhao, W., Hsu, S.N., Rajca, S., Calzolari, A., Boudouris, B.W., Casu, M.B., and Rajca, A. (2022). High-spin (S = 1) blatter-based diradical with robust stability and electrical conductivity. J. Am. Chem. Soc. *144*, 6059–6070. https://doi.org/10.1021/jacs.2c01141.

45. Junghoefer, T., Calzolari, A., Baev, I., Glaser, M., Ciccullo, F., Giangrisostomi, E., Ovsyannikov, R., Kielgast, F., Nissen, M., Schwarz, J., et al. (2022). Magnetic behavior in metal-free radical thin films. Chem *8*, 801–814. https://doi.org/10.1016/j.chempr.2021.11.021.

46. Shu, C., Pink, M., Junghoefer, T., Nadler, E., Rajca, S., Casu, M.B., and Rajca, A. (2021). Synthesis and thin films of thermally robust quartet (S = 3/2) ground state triradical. J. Am. Chem. Soc. *143*, 5508–5518. https://doi.org/10.1021/jacs.1c01305.

47. Shu, C., Zhang, H., Olankitwanit, A., Rajca, S., and Rajca, A. (2019). High-spin diradical dication of chiral π-conjugated double helical molecule. J. Am. Chem. Soc. *141*, 17287–17294. https://doi.org/10.1021/jacs.9b08711.

48. Yu, I., Jo, Y., Ko, J., Kim, D.Y., Sohn, D., and Joo, Y. (2020). Making nonconjugated small-molecule organic radicals conduct. Nano Lett. *20*, 5376–5382. https://doi.org/10.1021/acs.nanolett.0c01730.

49. Jo, Y., Yu, I., Ko, J., Kwon, J.E., and Joo, Y. (2022). Sequential codoping making nonconjugated organic radicals conduct ionically electronically. Small Sci. *2*, 2100081. https://doi.org/10.1002/smsc.202100081.

50. Ratera, I., and Veciana, J. (2012). Playing with organic radicals as building blocks for functional molecular materials. Chem. Soc. Rev. *41*, 303–349. https://doi.org/10.1039/c1cs15165g.

51. Gallagher, N.M., Olankitwanit, A., and Rajca, A. (2015). High-spin organic molecules. J. Org. Chem. *80*, 1291–1298. https://doi.org/10.1021/jo502505r.

52. Tan, Y., Hsu, S.N., Tahir, H., Dou, L., Savoie, B.M., and Boudouris, B.W. (2022). Electronic and spintronic open-shell macromolecules, Quo vadis? J. Am. Chem. Soc. *144*, 626–647. https://doi.org/10.1021/jacs.1c09815.

53. Deumal, M., Vela, S., Fumanal, M., Ribas-Arino, J., and Novoa, J.J. (2021). Insights into the magnetism and phase transitions of organic radical-based materials. J. Mater. Chem. C *9*, 10624–10646. https://doi.org/10.1039/d1tc01376a.

54. Kumar, S.K.M., Bhat, B.V., Keshri, S.K., and Mukhopadhyay, P. (2016). Recent advances in organic radicals and their magnetism. Immunol. Lett. *173*, 42–54. https://doi.org/10.3390/magnetochemistry2040042.

55. Nakabayashi, K., Kawano, M., Yoshizawa, M., Ohkoshi, S.I., and Fujita, M. (2004). Cavity-induced spin-spin interaction between organic radicals within a self-assembled coordination cage. J. Am. Chem. Soc. *126*, 16694–16695. https://doi.org/10.1021/ja044445p.

56. Li, D., and Yu, G. (2021). Innovation of materials, devices, and functionalized interfaces in organic spintronics. Adv. Funct. Mater. *31*, 2100550. https://doi.org/10.1002/adfm.202100550.

57. Adams, D.J., Mayer, K.S., Steelman, M., and Azoulay, J.D. (2022). Magnetic characterization of open-shell donor–acceptor conjugated polymers. J. Phys. Chem. C *126*, 5701–5710. https://doi.org/10.1021/acs.jpcc.1c10020.

58. Gu, H., Zhang, X., Wei, H., Huang, Y., Wei, S., and Guo, Z. (2013). An overview of the magnetoresistance phenomenon in molecular systems. Chem. Soc. Rev. *42*, 5907–5943. https://doi.org/10.1039/c3cs60074b.

59. Sugawara, T., Komatsu, H., and Suzuki, K. (2011). Interplay between magnetism and conductivity derived from spin-polarized donor radicals. Chem. Soc. Rev. *40*, 3105–3118. https://doi.org/10.1039/c0cs00157k.

60. Hayakawa, R., Karimi, M.A., Wolf, J., Huhn, T., Zöllner, M.S., Herrmann, C., and Scheer, E. (2016). Large magnetoresistance in single-radical molecular junctions. Nano Lett. *16*, 4960–4967. https://doi.org/10.1021/acs.nanolett.6b01595.

61. Docherty, R., Clydesdale, G., Roberts, K.J., and Bennema, P. (1991). Application of bravais-friedel-donnay-harker, attachment energy and Ising models to predicting and understanding the morphology of molecular crystals. J. Phys. D Appl. Phys. *24*, 89–99. https://doi.org/10.1088/0022-3727/24/2/001.

62. Kemper, T.W., Larsen, R.E., and Gennett, T. (2014). Relationship between molecular structure and electron transfer in a polymeric Nitroxyl-radical energy storage material. J. Phys. Chem. C *118*, 17213–17220. https://doi.org/10.1021/jp501628z.

63. Kemper, T.W., Larsen, R.E., and Gennett, T. (2015). Density of states and the role of energetic disorder in charge transport in an organic radical polymer in the solid state. J. Phys. Chem. C *119*, 21369–21375. https://doi.org/10.1021/acs.jpcc.5b06368.

64. Stallinga, P. (2011). Electronic transport in organic materials: comparison of band theory with percolation/(variable range) hopping theory. Adv. Mater. *23*, 3356–3362. https://doi.org/10.1002/adma.201101129.

65. Shklovskii, B.I., and Efros, A.L. (1984). Variable-Range Hopping Conduction (Springer Science & Business Media), pp. 202–227. https://doi.org/10.1007/978-3-662-02403-4_9.

66. Xie, J., Ewing, S., Boyn, J.N., Filatov, A.S., Cheng, B., Ma, T., Grocke, G.L., Zhao, N., Itani, R., Sun, X., et al. (2022). Intrinsic glassy-metallic transport in an amorphous coordination polymer. Nature *611*, 479–484. https://doi.org/10.1038/s41586-022-05261-4.

67. Karlsson, C., Suga, T., and Nishide, H. (2017). Quantifying TEMPO redox polymer charge transport toward the organic radical battery. ACS Appl. Mater. Interfaces *9*, 10692–10698. https://doi.org/10.1021/acsami.7b00403.

68. Liang, Z., Tan, Y., Hsu, S.N., Stoehr, J.F., Tahir, H., Woeppel, A.B., Debnath, S., Zeller, M., Dou, L., Savoie, B.M., and Boudouris, B.W. (2023). Charge transport and antiferromagnetic ordering in nitroxide radical crystals. Mol. Syst. Des. Eng. *8*, 464–472. https://doi.org/10.1039/d2me00202g.

69. Hay, M.E., Hui Wong, S., Mukherjee, S., and Boudouris, B.W. (2017). Controlling open-shell loading in norbornene-based radical polymers modulates the solid-state charge transport exponentially. J. Polym. Sci., Part B: Polym. Phys. *55*, 1516–1525. https://doi.org/10.1002/polb.24406.

70. Nakatsuji, S., Mizumoto, M., Kitamura, K., Akutsu, H., and Yamada, J.I. (2001). Preparation and properties of biphenyl and cholesterol derivatives with nitroxide radicals. Mol. Cryst. Liq. Cryst. Sci. Technol. Sect. A Mol. Cryst. Liq. Cryst. *356*, 33–40. https://doi.org/10.1080/10587250108023684.

71. Coleman, L.B. (1975). Technique for conductivity measurements on single crystals of organic materials. Rev. Sci. Instrum. *46*, 1125–1126. https://doi.org/10.1063/1.1134370.

72. Kresse, G., and Furthmüller, J. (1996). Efficient iterative schemes for ab initio total-energy calculations using a plane-wave basis set. Phys. Rev. B Condens. Matter *54*, 11169–11186. https://doi.org/10.1103/PhysRevB.54.11169.

73. Kresse, G., and Furthmüller, J. (1996). Efficiency of ab-initio total energy calculations for metals and semiconductors using a plane-wave basis set. Comput. Mater. Sci. *6*, 15–50. https://doi.org/10.1016/0927-0256(96)00008-0.

74. Kresse, G., and Hafner, J. (1994). Ab initio molecular-dynamics simulation of the liquid-metalamorphous- semiconductor transition in germanium. Phys. Rev. B *49*, 14251–14269. https://doi.org/10.1103/PhysRevB.49.14251.

75. Kresse, G., and Hafner, J. (1993). Ab initio molecular dynamics for liquid metals. Phys. Rev. B *47*, 558–561. https://doi.org/10.1103/PhysRevB.47.558.

76. Kresse, G., and Joubert, D. (1999). From ultrasoft pseudopotentials to the projector augmented-wave method. Phys. Rev. B *59*, 1758–1775. https://doi.org/10.1103/PhysRevB.59.1758.

77. Wang, V., Xu, N., Liu, J.C., Tang, G., and Geng, W.T. (2021). VASPKIT: a user-friendly interface facilitating high-throughput computing and analysis using VASP code. Comput. Phys. Commun. *267*, 108033. https://doi.org/10.1016/j.cpc.2021.108033.

78. Spackman, P.R., Turner, M.J., McKinnon, J.J., Wolff, S.K., Grimwood, D.J., Jayatilaka, D., and Spackman, M.A. (2021). *CrystalExplorer*: a program for Hirshfeld surface analysis, visualization and quantitative analysis of molecular crystals. J. Appl. Cryst. *54*, 1006–1011. https://doi.org/10.1107/S1600576721002910.

79. Khot, A., and Savoie, B.M. (2021). Top-down coarse-grained framework for characterizing mixed conducting polymers. Macromolecules *54*, 4889–4901. https://doi.org/10.1021/acs.macromol.1c00219.